A space qualified digital imaging platform: design, TVAC characterization, and radiation performance with the HWK4123 sCMOS sensor

Olivier Daigle[a], Émile Beaulieu[a], Deren Mehmet[b], and Hank Hu[b]

[a]Nüvü, 603-355 Peel St., Montréal, Qc, Canada
[b]Fairchild Imaging, 1841 Zanker Road Suite 50, Can Jose, CA, USA

ABSTRACT

We present the characterization results of Nüvü Camēras' space-qualified digital imaging platform, integrated with the Fairchild Imaging's low noise (<0.3ē RMS) HWK4123 9.4-megapixel sCMOS sensor. The imaging system has been designed for challenging missions requiring low read noise and/or high dynamic range, such as SSA, transient imaging, or applications requiring daytime and nighttime imaging capability. Environmental testing was performed in TVAC to evaluate performance stability over the imaging system's full temperature range. In addition, we present radiation response data obtained during a proton irradiation campaign conducted at TRIUMF (British Columbia, Canada), focusing on TID, and single-event phenomena observed in the HWK4123 sensor. These results demonstrate the suitability of the Nüvü-Fairchild Imaging innovative devices for space missions requiring high-performance wide-field sensing.

Keywords: Manuscript format, template, SPIE Proceedings, LaTeX

1. INTRODUCTION

The modern history of solid-state image sensors begins with the dominance of the Charge Coupled Device (CCD), widely adopted from the 1970s onward for scientific and early digital imaging. CCDs offered excellent uniformity, low noise, and high image quality, which made them the preferred technology for astronomy, broadcast video, and early digital cameras. At the same time, Fairchild Semiconductor Company was working on the Complementary Metal Oxide Semiconductor (CMOS) process technology, which eventually led Radio Corporation of America (RCA) to propose solid-state image sensors using thin-film transistors. However, the first CMOS image sensors, based on passive pixel architectures, suffered from high noise and poor image fidelity due to the lack of in-pixel signal amplification. Although proposed in 1968 by Noble,[1] the Active-Pixel Sensor (APS) technology, exhibiting an amplifier in every pixel, had to wait until the Metal Oxide Semiconductor Field-Effect Transistor (MOSFET) semiconductor fabrication processes reached sub-micron levels during the 1980s before it could be fabricated. By the early 1990s, several Japanese and American companies had developed practical MOS APS products.

The key turning point came in the early 1990s with the advent of the CMOS APS[2] which introduced in-pixel amplification and Correlated Double Sampling (CDS) to reduce noise while enabling "camera-on-a-chip" integration. That technology advance further led to rapid architectural improvements such as pinned photodiodes, shared readout structures, and on-chip signal processing, closing the performance gap with CCDs while preserving CMOS advantages in power consumption, speed, and manufacturability. Ultimately, they provoked the digital imaging revolution of the 2000s.

In parallel, a distinct "Scientific CMOS" (sCMOS) trajectory emerged in the 2000s by a consortium of three companies: Fairchild Imaging, Andor Technology, and PCO, targeting applications in microscopy, astronomy, and space instrumentation. With the technology enabling sufficiently small capacitors for the charge-voltage conversion, CDS and column-parallel Analog to Digital Converters (ADCs), the new device achieved both low noise read-out and fast frame rates that were, and still are, together unachievable with the CCD technology. Large formats, continued innovations such as back-side illumination, deep depletion, and radiation-hardened designs have enabled CMOS sensors to penetrate even the most demanding scientific and space applications.

Further author information: (Send correspondence to Olivier Daigle)
Olivier Daigle: E-mail: odaigle@nuvucameras.com, Telephone: +1 514 733 8666 x1001

Today, this evolution continues with devices like the Fairchild HWK4123. The HWK4123 is an ultra-low noise Backside Illuminated (BSI) Scientific CMOS (sCMOS) image sensor optimized for rolling shutter operation. It is based on a 5T pixel with dual gains, the main imaging array size is 4100 columns by 2300 rows, forming a 4/3" optical format (4.6μm pixels). Advanced features include dark columns and injection rows for improved noise performance and internal and external triggers options. The HWK4123 can run at 120fps at full frame single gain mode. Sensor control is through a SPI interface, and output is via sLVDS. The sensor achieves sub-electron read noise (<0.3$\bar{e}$ RMS), low dark current (<0.1$\bar{e}$/pixel/s @0°C), and high dynamic range (>83 dB with dual-gain). With such characteristics, the device enables photon-resolving capability, high full well, and high frame rate, all at the same time. These characteristics challenge what extreme low noise devices like the Electron Multiplying CCD (EMCCD) are capable of, which led Nüvü Camēras to develop a space-qualified digital imaging platform to support CMOS and sCMOS sensors in general, and chose the HWK4123 as the first device to be supported.

In this paper, we present Nüvü Camēras' new space-qualified imaging platform (Section 2), Thermal Vacuum Chamber (TVAC) characterization data obtained with the HWK4123 sensor (Section 4), and results from a proton irradiation campaign of the HWK4123 (Section 5).

2. A NEW SPACE DIGITAL IMAGING PLATFORM

Nüvü Camēras' space-qualified digital imaging platform builds upon the company's heritage EMCCD/CCD space imaging platform,[3] itself derived from the Camera Proximity Electronics (CPE) developed for the two cameras of the Nancy Grace Roman Space Telescope (Roman) Coronagraph Instrument (CGI)[4] and from a development for the Canadian Space Agency (CSA).[5] The platform was conceived as a generic architecture capable of supporting multiple CMOS image sensors, with the HWK4123 being the first implementation.

2.1 System requirements

The system was designed to meet the high-level requirements depicted in Table 1. The CubeSat standard was adopted as the envelope of the system, and a goal was set to make the imaging system, excluding the optical payload, smaller than 1U. The mechanical requirements are listed in Table 2. This was deemed enough volume to accommodate a stack of three Printed Circuit Boards (PCBs) (See section 2.2).

In order to easily integrate into a small spacecraft, the power requirement had to be kept low, and the system had to be powered by a single input voltage (Table 3). Moreover, since the data rate of CMOS sensors can be very high, it was decided to have a volatile storage on the controller to absorb bursts of images. The buffered images can then be transmitted at a slower rate through the communication interface. The baseline communication interface is CameraLink, from base to full variants, which allows a full frame rate between 8 and $\sim$50 fps to be transmitted. A support for CameraLink HS, that will allow the full frame rate of the sensor to be used continuously, is in development. Regardless of the communication interface, the camera can append a telemetry line to every transmitted image, providing real-time access to the system status and health information.

The environmental requirements were defined for a Low Earth Orbit (LEO) spacecraft (Table 4). The Total Ionizing Dose (TID) and SEL_{LET} thresholds imply the system is designed with radiation-tolerant and space-qualified IEEE parts. The TID requirement of $\geq$15krad is defined as the dose the electronic components shall support natively, without shielding. Shielding can be used to increase the total dose the system can sustain. Compliance with the radiation requirements was demonstrated through radiation analysis and component selection.

2.2 Design

The system is made to easily integrate with several CMOS and sCMOS sensors. In order to accomplish this, a base system was designed, comprising a stack of two PCBs. Then, a third PCB, being rigid or flex-rigid, implements the support for a particular sensor, through a high-density connector. The two PCBs of the base system are:

1. A power supply board, which takes the spacecraft bus power and converts it into the required secondary voltages;
2. A digital board, which houses the digital core of the electronic controller, providing all of the required Input-Outputs (I/Os) to the CMOS sensor, together with the telemetry measurements and fault handling (temperature, voltage, current, and others) for the base components.

Table 1: System requirements

Parameter	Type	Value	ID
Resolution	Spatial	2415 (h)	SYS_RES_1
Resolution	Spatial	4656 (v)	SYS_RES_2
Resolution	Temporal	120 fps	SYS_RES_3
Resolution	Digital	12 bits	SYS_RES_4
Telemetry	Digital	Present	SYS_TLM_1
Imaging	Read-out	$<$0.4 $\bar{e}$	SYS_NOISE_1
Imaging	Thermal	$<$2 $\bar{e}$/sec	SYS_NOISE_2
Imaging	Linearity	$<$1 %	SYS_PIX_1
Imaging	Full well	$\geq$7 k$\bar{e}$	SYS_PIX_2

Table 2: Mechanical requirements

Parameter	Type	Value	ID
Dimension	Volume	$\leq$10 $\times$10 $\times$6 cm^3	MEC_DIM_1
Dimension	Mass	$\leq$1.0 kg	MEC_DIM_2

Table 3: Electrical requirements

Parameter	Type	Value	ID
Power	Input voltage	16–28 V	ELE_PWR_1
Power	Nominal power	$<$10 W	ELE_PWR_2
Storage	Non-volatile storage	256 Mbits	ELE_STOR_1
Storage	Volatile storage	112 images	ELE_STOR_2

Table 4: Environmental requirements

Parameter	Type	Value	ID
Radiation	Total dose	$\geq$15 krad	ENV_RAD_1
Radiation	SEL_{LET} threshold	$\geq$60 MeV·cm^2/mg	ENV_RAD_2
Thermal	Non-operational temperature range	-40 – +60 °C	ENV_THE_1
Thermal	Operational temperature range	-35 – +60 °C	ENV_THE_2
Pression	Operating pressure	Vacuum	ENV_PRE_1
Vibrations	Random vibrations	6.8 g RMS @ 1 minute/axis, 20-2000 Hz	ENV_VIB_1

2.2.1 Power supply

The power supply module converts the 16–28V spacecraft bus voltage into the secondary supply rails required to operate the CPE. These voltages are generated by Switched Mode Power Supplies (SMPS) synchronized to the image readout by the Field Programmable Gate Array (FPGA), ensuring that any residual switching artifacts remain spatially fixed within the acquired images and can therefore be removed through bias-frame subtraction.

In addition, the power supply module provides an adjustable 0–-15,V output capable of driving either a heater or a Thermoelectric Cooler (TEC), enabling closed-loop temperature regulation of the CMOS sensor.

2.2.2 Digital core

The digital core is based on Microchip's radiation-tolerant PolarFire FPGA. As a flash-based device, the FPGA is immune to configuration upsets for particles with a Linear Energy Transfer (LET) below 80 MeV·cm^2/mg. It is qualified for TID levels exceeding 100 krad(Si) and incorporates built-in Single Error Correction, Double Error Detection (SECDED) protection for its memory resources. The device supports up to 24 high-speed serial transceiver lanes operating at up to 10,Gbit/s, which can be used to interface with the CMOS sensor or with external communication links.

The FPGA exposes the following digital resources to the CMOS sensor:

- 60 Low-voltage differential signaling (LVDS) pairs operating at up to 1.25 Gbit/s;
- 24 LVCMOS 1.8,V signals operating at up to 500 Mbit/s;
- 4 LVCMOS 2.5,V signals operating at up to 500 Mbit/s;
- 16 high-speed serial receiver pairs operating at up to 10.3125 Gbit/s;
- 8 General Purpose I/O (GPIO) signals operating at up to 66 Mbit/s and intended for a Serial Peripheral Interface (SPI) interface.

The digital core currently supports the Camera Link protocol in all configurations, from base to full. Support for Camera Link HS is under development. The architecture is sufficiently flexible to accommodate additional communication interfaces, including Gigabit Ethernet, 10 Gigabit Ethernet, SpaceWire, and other protocols as required by the mission.

2.2.3 Analog core

The analog core consists mainly of the generation of low power bias levels and a few higher power supply voltages. The digital board has provision for generating the following

- A total of 12 Direct Current (DC) -5–5V DC levels with a resolution of 12 bits that can then be scaled to the required levels by circuitry on the sensor-specific headboard;
- 4 Low-Dropout regulators (LDOs) with a maximum output current capability in excess of 1 A.

2.2.4 Latch-up protection

The system is designed to support both space-qualified and commercial image sensors. While the radiation response of space-qualified devices is generally well characterized, commercial sensors may exhibit unknown behaviour under irradiation, including susceptibility to latch-up events. To mitigate this risk, the CPE incorporates multiple protection mechanisms:

- All low-power bias rails are voltage-monitored and current-limited. Overcurrent conditions are detected indirectly through the resulting voltage drop on the monitored rail. Although the telemetry system response time is on the order of several tens of milliseconds, the current-limiting circuitry prevents excessive power dissipation, thereby avoiding damage to the sensor while the CPE detects and recovers from the latch-up condition.
- All high-power supply rails are monitored using sense resistors and high-speed comparators. The comparator outputs are connected directly to the FPGA, enabling near-immediate detection of overcurrent conditions. Upon detection, the FPGA can rapidly disable the sensor power supplies, minimizing the duration and potential impact of the latch-up event.

3. INTEGRATION WITH THE HWK4123

As the first image sensor supported by the platform, the HWK4123 served as a representative implementation used to validate the architecture and its adaptability to future devices. The integration effort encompassed the development of the sensor-specific electrical interfaces, control logic, timing generation, and data acquisition firmware required for nominal operation. This section presents the resulting implementation made to support the HWK4123.

3.1 Supported read-out modes

The HWK4123 read-out implementation was limited to two operating modes, 120 fps and 5 fps. These configurations were selected to span the primary operational regimes of interest, namely high-speed acquisition and low-noise imaging under reduced read-out bandwidth conditions. Both modes support either fixed-gain operation or automatic gain selection for High Dynamic Range (HDR) imaging. Although a global shutter mode exists, all supported configurations employ a rolling-shutter read-out architecture to take advantage of the capability of the device to yield sub-electron read-out noise.

3.2 Sub-electron read-out noise

As shown in Section 4, the system achieves a sub-electron read-out noise when operated with a gain of 32. This level of performance enables single-photon resolution at read-out speeds that are beyond the capabilities of conventional CCD technology. As an illustration, Figure 1 presents the histogram of pixel values acquired under low-light illumination, at room temperature, in which the peaks corresponding to successive photon events are clearly resolved.

4. TVAC CHARACTERIZATION RESULTS

TVAC testing was performed to characterize the HWK4123 imaging system under representative space operating conditions. The study focuses on the dependence of key performance metrics – read-out noise, linearity, and dark current – on system temperature, with the sensor and electronics maintained at a common thermal interface. The results presented in the following sections summarize the system behaviour across the investigated thermal range. For these tests, only fixed-gain read-out modes were executed.

4.1 Read-out noise

The Read-out Noise (RON) and full well are measured using the Photon Transfer Curve (PTC) method.[6] A stabilized light source is used to uniformly illuminate the sensor while the exposure time is progressively increased, thereby varying the number of accumulated photoelectrons. This method simultaneously yields the reciprocal system gain (k-gain), while the linearity is assessed from the proportionality between the measured signal and the exposure time. Owing to process-induced device variations inherent to the pixel-parallel architecture of CMOS image sensors, each pixel exhibits a slightly different conversion gain and read-out characteristics. These variations arise primarily from small differences in the floating diffusion capacitance and in the characteristics of the in-pixel read-out circuitry. Consequently, the k-gain, RON, and linearity are evaluated on a per-pixel basis, enabling the spatial distribution of these parameters across the sensor to be characterized. As a result, this per-pixel analysis also enables the generation of the read-out noise distribution (Figure 2).

The read-out noise achieved is comparable to the specification quoted by Fairchild.

4.2 Linearity

The HWK4123 linearity was found to be almost independent of temperature, as shown in Figure 3, with no systematic variation observed over the investigated thermal range. The only obvious trend is a slightly larger signal range within the $\pm 1\%$ range at gain of 32 for warmer temperatures.

4.3 Dark current

The HWK4123 dark current was measured to be as specified by Fairchild on un-radiated devices. See Section 5.4 for a comparison of pre- and post-radiation dark current data as a function of the device temperature.

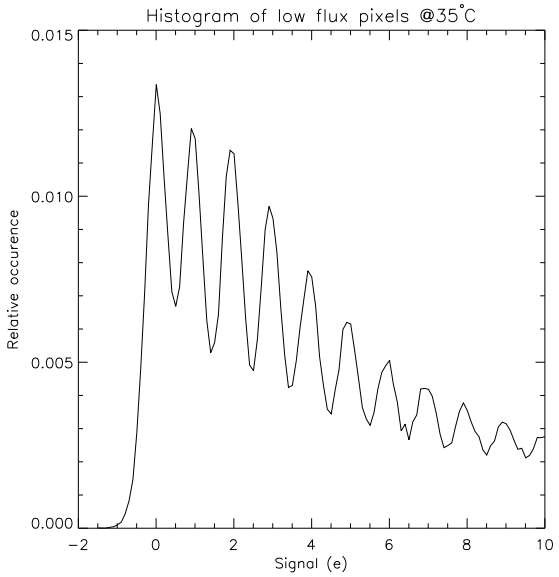

Figure 1: Histogram of low flux pixels at 5 fps and gain of 32, showing the photon-resolving capability of the device even when operated at room temperature.

Table 5: Read-out noise at 5 fps, unity gain (ē)

Temperature (°C)	10%	50%	90%
-20	1.906	2.096	2.276
-10	1.915	2.125	2.305
10	1.946	2.156	2.336
20	2.031	2.211	2.391

Table 6: Read-out noise at 5 fps, gain 32 (ē)

Temperature (°C)	10%	50%	90%
-20	0.212	0.272	0.362
-10	0.230	0.290	0.380
10	0.245	0.295	0.385
20	0.244	0.304	0.384

Table 7: Read-out noise at 120 fps, unity gain (ē)

Temperature (°C)	10%	50%	90%
-20	5.540	5.880	6.320
-10	5.627	5.987	6.467
10	5.794	6.174	6.624
20	5.967	6.347	6.797

Table 8: Read-out noise at 120 fps, gain 32 (ē)

Temperature (°C)	10%	50%	90%
-20	0.327	0.417	0.537
-10	0.335	0.425	0.545
10	0.354	0.434	0.554
20	0.376	0.446	0.566

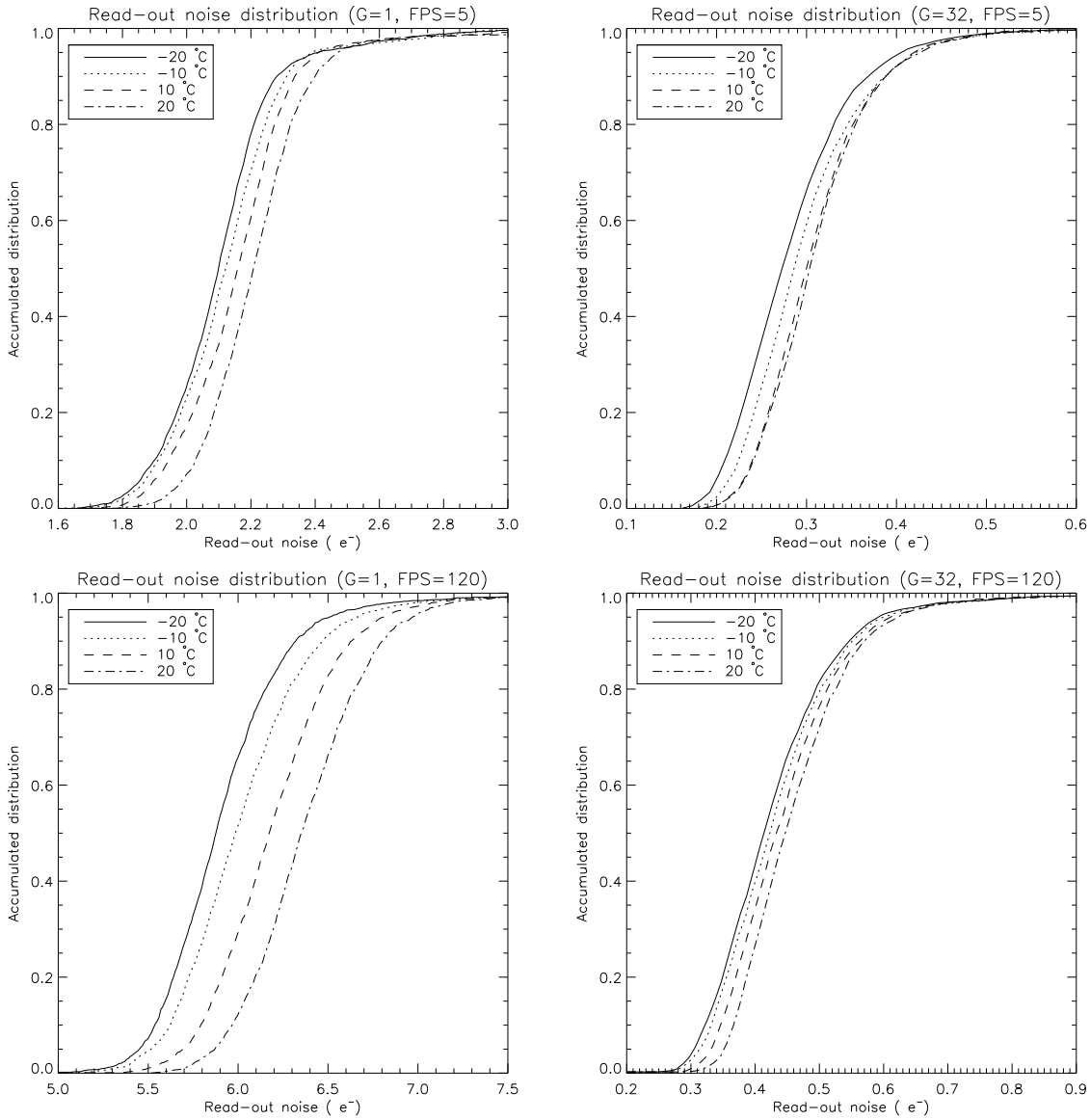

Figure 2: Read-out noise distribution as a function of the temperature of the system, the read-out speed and the gain of the HWK4123. Values for the 10, 50 and 90% distributions are depicted in Tables 5–8.

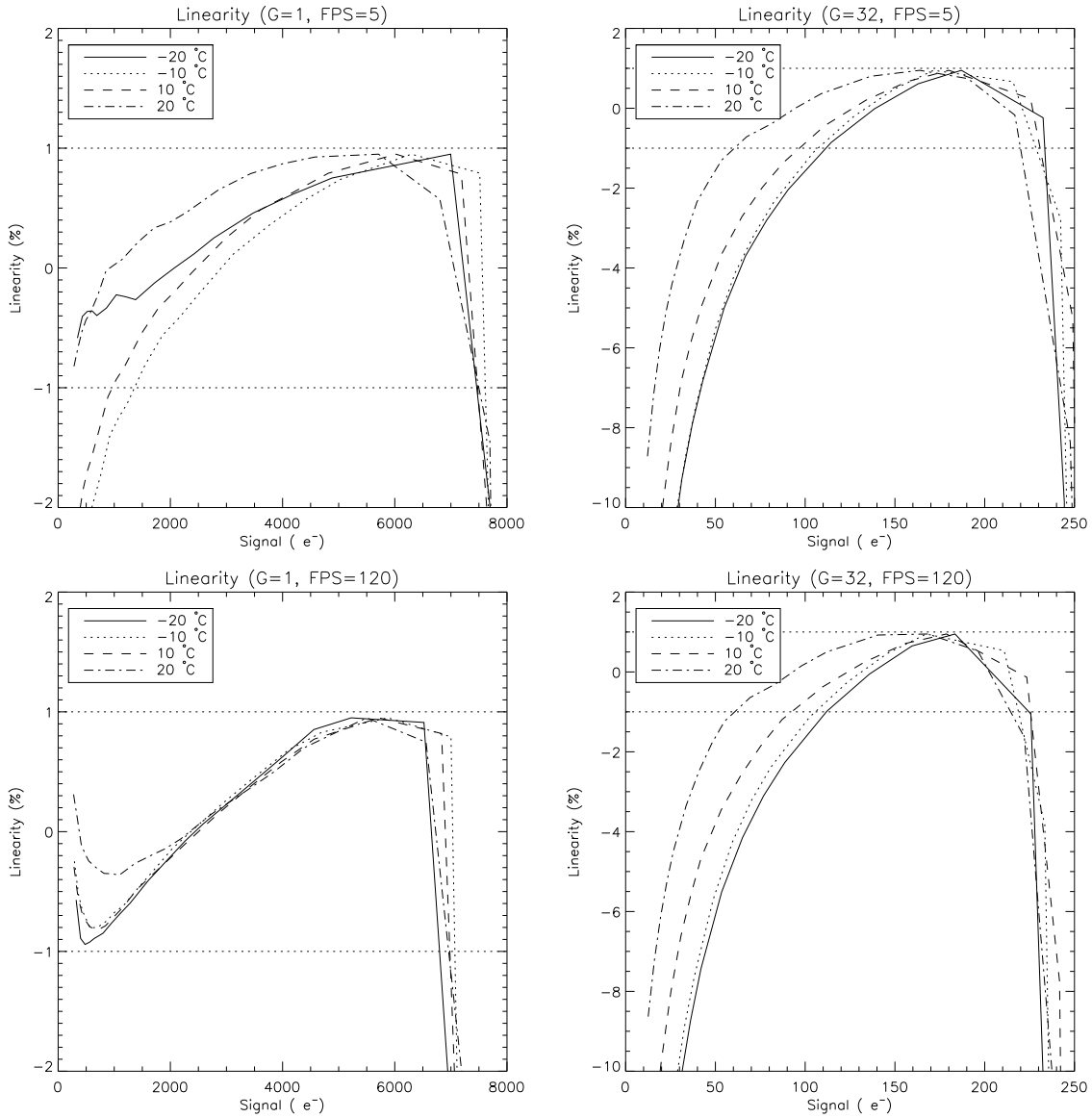

Figure 3: System's response linearity as a function of the temperature of the system, the read-out speed and the gain of the HWK4123.

5. PROTON IRRADIATION CAMPAIGN

As reported in [7], heavy ion testing was executed on the HWK4123 at UCL Louvain-la-Neuve with LET ranging from 1.3 to 62.5 MeV·cm^2/mg. Although no catastrophic failure of the device was experimented, Single-event Functional Interrupts (SEFIs) did occur, with the most severe one leading to the loss of the video streaming. A power cycle was sufficient to restore operation.

On the other hand, TID exposure can progressively damage a CMOS image sensor by trapping charge in the oxide layers and at semiconductor interfaces, which alters transistor threshold voltages, increases leakage currents, degrades charge transfer and readout circuitry, and ultimately raises dark current, hot-pixel count, temporal noise, and fixed-pattern noise while potentially reducing dynamic range and image uniformity. In space environments, where sensors are continuously exposed to ionizing radiation from trapped particles, solar events, and cosmic rays, these cumulative effects can significantly impair imaging performance and mission lifetime. Assessing TID sensitivity is therefore essential to predict long-term operability, establish shielding and calibration requirements, validate mission suitability for a given orbit, and ensure that instruments maintain acceptable performance throughout their operational life. Since no published data exists on the impact of TID on the HWK4123, a proton radiation campaign was executed.

Two sensors were irradiated at the TRIUMF facility in Vancouver, BC, in December 2025 with proton energies ranging from 20 to 105 MeV. Both sensors were irradiated to a total dose of 50 krad. A summary of the radiation campaign for both sensors is depicted in Tables 9 and 10.

Prior to the radiation campaign, a complete characterization of the devices was made at Nüvü, with the parameters described in Section 4 being measured. Those were measured again once the sensors were recovered, one month after the radiation campaign was finished, as the sensors needed to ”cool down” before they were allowed to leave TRIUMF.

5.1 Experimental set-up

Although it is the same hardware that was used at the irradiation facility as what usually composes a nüSpace camera, the HWK4123 and the driving electronics had to be separated so that only the HWK4123 would be irradiated. As shown in Figure 4, the set-up at TRIUMF consisted of the standard Nüvü HWK4123 headboard, connected to the Nüvü digital imaging controller through a custom extender board (Figure 4). The HWK4123 was covered with a 6.35 mm thick PEEK plate to avoid dust from reaching the sensor and shield it from residual light in the irradiation room so that unsaturated could be acquired. The plate had a negligible impact on the delivered dose.

The standard CameraLink interface of the system was used to carry images and receive commands to/from the controlling computer. In order to avoid running a CameraLink cable through the walls, a Pleora Technologies iPORT CL-GigE converter was used so that an Ethernet cable that was already available could be used. The controlling computer ran the Nüvü Software Development Kit (SDK) and acquisition suite.

The controller used for the radiation campaign ran a custom version of the Embedded Software (E-SW) and VHSIC Hardware Description Language (VHDL) code. That custom firmware allowed for extra monitoring of the sensor’s health. For instance, the current draw of every DC-level supply was monitored (Table 13), and the HWK4123’s configuration memory was constantly scrubbed to detect Single Event Upsets (SEUs). Through the fault handling mechanism of the E-SW, faults were defined so that automatic actions would be taken by the controller should any of the following occur:

- A configuration bit was flipped;
- The current of a monitored supply increased beyond a preset threshold;
- A desynchronization is detected on any of the 16 data lanes between the sensor and the FPGA;
- A time-out occurred when expecting an image from the HWK4123.

If any of those events occurred, the event was counted and a power cycle of the Device Under Test (DUT) was performed. This ensured the whole configuration and functional state of the device was recovered. The whole power cycle and reconfiguration process took about 100 ms. A provision was kept in the E-SW to disable the automatic power cycle of the device, should the fault rate be too high.

During all phases of the radiation campaign (Tables 9 and 10), the sensors were powered and were being read-out constantly at a rate of 1 fps in the 5 fps mode and at a gain of 32 (see Section 3.1) with the Nüvü's NüSpace read-out electronics. Between every radiation dose, 250 images were gathered in dark conditions at each of 0-s and 1-s integration times, at gain of 32 and 1, respectively.

The sensors were in the ambient atmosphere for the whole duration of the tests. Since they dissipate close to 2 W of heat, their temperature was stabilized to ∼35°C with a fan that ran in closed loop.

5.2 SEEs

The HWK4123 was monitored during the irradiation for Single-event Effects (SEEs). Those included SEUs on the configuration registers, desynchronizations of the digital video lines and image shifts induced by missing lines or partial lines being transferred.

5.2.1 SEUs

Continuous scrubbing of the HWK4123 configuration memory enabled the number of configuration SEUs to be quantified at each step of the radiation campaign. The results are shown in Figure 5 and Tables 11 and 12. The observed upset rate is low and operationally manageable, corresponding to approximately one configuration upset per month for a typical LEO mission environment.

The measured upset cross section is of the order of 2×10^{-10} SEU/proton/cm^2 for proton energies above 30 MeV. For proton energies below this threshold, the observed upset rate appears significantly lower; however, the available statistics are insufficient to confirm a dependence on energy in this regime.

5.2.2 Desynchronizations and data losses

The HWK4123 data stream incorporates dedicated Start Of Frame (SOF), Start Of Line (SOL), End Of Line (EOL), and End Of Frame (EOF) markers, enabling independent monitoring of the 16 video lanes between the sensor and the FPGA for synchronization integrity. Only 12 lane desynchronization events were observed for the first sensor and 5 for the second sensor over the entire acquisition campaign. The vast majority of these events occurred at 63 MeV; however, the statistics collected at the other beam energies are insufficient to draw conclusions regarding their relative prevalence.

In addition, the sensor appends a set of trailing pixels to each image line, with these pixels having a nominal value of 1. For the final two image lines, the corresponding trailing pixels are assigned a value of 1025. These deterministic sentinel values provide a means of verifying the spatial alignment of the received image data and detecting any pixel-shift anomalies introduced during transmission. Across the datasets acquired from the two sensors under test, only a single image-shift event was observed. It occurred at a proton energy of 63 MeV, which is the energy at which the majority of the dose was accumulated. In itself, that event does not put a constraint on the most likely proton energy for that kind of event to occur.

5.3 Current consumption

The current consumption of the HWK4123 was measured while it was being irradiated with a resolution of 1 mA. Two different mechanisms were used to monitor the various currents. The low power supplies of the HWK4123 were directly measured by probing the voltage drop across a known resistor. This is what was used to monitor the currents listed in Table 13. The nominal current listed in the table is the one measured prior to the radiation.

The plots of the normalized currents for the low-power supplies as a function of the accumulated dose are shown in Figure 6. The observed fluctuations are entirely consistent with the 1 mA quantization of the current measurements, indicating no detectable change in the supply currents with accumulated dose.

The high current supplies were monitored conjointly by measuring the current at the output of the buck converter of the controller. While that way of measuring the current did not allow us to disentangle the current drawn by the different circuits of the HWK4123, it did allow us to detect current creeping that could occur with the accumulation of the dose. The supplies are separated in the following way:

- C3V3: Sum of the currents drawn by VTX2_POSH, AVDD_PIX, AVDD, and the digital core of the controller;

Table 9: Sensor 1

Type	Proton energy (MeV)	Time (min)	Flux 10^6 protons/s	Fluence (10^{10} protons)	Dose (krad(Si))	Accumulated dose (krad(Si))
SEU	20	50.5	3.3	1.0	4.64	4.6
SEU	27.1	17.0	9.8	1.0	3.79	8.4
SEU	35.5	31.5	5.3	1.0	2.82	11.2
SEU	63	16.7	10.0	1.0	1.33	12.5
TID	63	5.7	100.0	3.4	4.51	17
TID	63	10.7	100.0	6.4	8.49	25.5
TID	63	11.8	100.0	7.1	9.42	34.9
TID	63	12.6	100.0	7.6	10.01	44.9
TID	63	4.0	100.0	2.4	3.18	48.1
SEU	105	16.7	10.0	1.0	0.91	49
SEU	85.5	21.1	7.9	1.0	1.21	50.2

Table 10: Sensor 2

Type	Proton energy (MeV)	Time (min)	Flux 10^6 protons/s	Fluence (10^{10} protons)	Dose (krad(Si))	Accumulated dose (krad(Si))
SEU	105	16.7	10.0	1.0	0.91	0.9
SEU	85.5	21.1	7.9	1.0	1.21	2.1
SEU	63	16.7	10.0	1.0	1.36	3.5
SEU	35.5	17.2	9.7	1.0	2.89	6.4
SEU	27.1	21.7	7.7	1.0	3.88	10.3
SEU	20	16.8	9.9	1.0	4.64	14.9
TID	63	6.4	100.0	3.8	5.11	20
TID	63	12.6	100.0	7.5	10.0	30
TID	63	12.6	100.0	7.5	10.0	40
TID	63	12.6	100.0	7.5	10.0	50

Table 11: Sensor 1 SEEs.

Energy (MeV)	SEU	SEU/ proton/cm^2	Desync.	Desync./ proton/cm^2	Shift	Total dose (krad)
20.0	1	1.0E-10	0	0.0	0	4.6
27.1	1	1.0E-10	0	0.0	0	3.8
35.5	2	2.0E-10	1	1.0E-10	0	2.8
63.0	53	1.9E-10	10	3.6E-11	0	36.9
85.5	2	2.0E-10	0	0.0	0	1.2
105.0	2	2.0E-10	1	1.0E-10	0	0.9

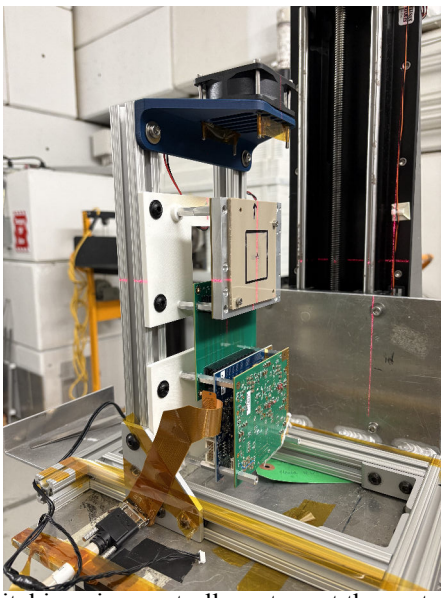

Figure 4: HWK4123 headboard and digital imaging controller set-up at the proton irradiation facility, during beam alignment. The sensor is behind the beige PEEK cover to prevent dust from reaching it. The NüSpace CMOS controller is seen below and the cooling fan is seen above. A flex PCB handles the CameraLink communication.

Table 12: Sensor 2 SEEs.

Energy (MeV)	SEU	SEU/ proton/cm^2	Desync.	Desync./ proton/cm^2	Shift	Total dose (krad)
20.0	0	0.0	0	0.0	0	4.6
27.1	0	0.0	0	0.0	0	3.9
35.5	5	4.9E-10	0	0.0	0	2.9
63.0	53	2.5E-10	4	1.9E-11	1	36.5
85.5	0	0.0	0	0.0	0	1.2
105.0	1	1.0E-10	1	1.0E-10	0	0.9

Table 13: Pre-irradiation HWK4123 low power supply current consumption. At the mA level, the pre-radiation current consumption of the two sensors is the same.

Input	Sensor 1 nominal current (A)	Sensor 2 nominal current (A)
VRST_DR1	0.003	0.003
VRST_DR0	0.001	0.001
VRST_POS	0.003	0.003
VSEL_POS	0.004	0.004
VTX1_POS	0.002	0.002
VTX2_POSL	0.000	0.000
VRST_INJ	0.000	0.000
AVDD_BB	0.013	0.013
VRST_NEG	-0.008	-0.008
VTX1_NEGL	0.002	0.002
VTX2_NEG	0.006	0.006

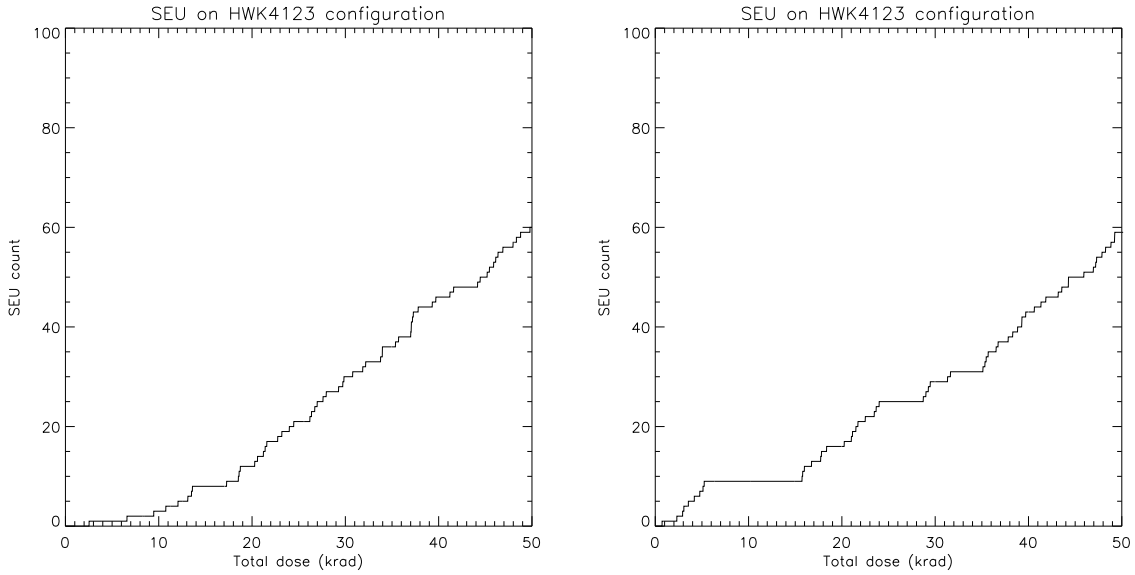

Figure 5: Sum of the SEUs recorded for the configuration of each DUT as a function of the accumulated dose. **Left**: Sensor 1. **Right**: Sensor 2.

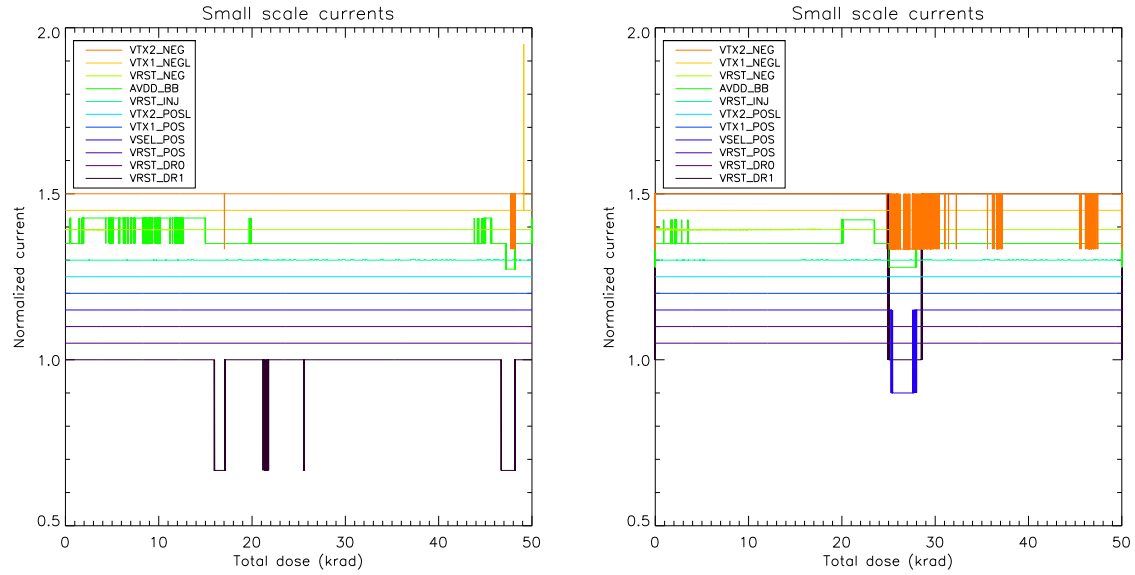

Figure 6: Normalized small-scale currents as a function of the accumulated dose. Currents are offset by steps of 0.05 for more clarity. **Left**: Sensor 1. **Right**: Sensor 2.

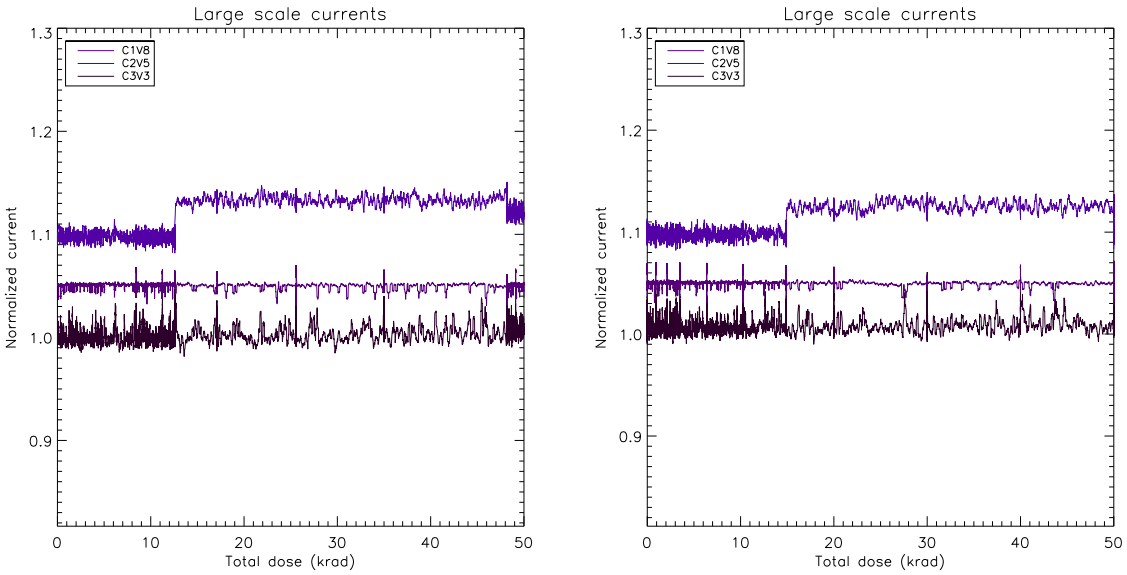

Figure 7: Large scale currents as a function of the accumulated dose. Currents are offset by steps of 0.05 for more clarity. **Left**: Sensor 1. **Right**: Sensor 2.

- C2V5: The current drawn by VDDIO;
- C1V8: Sum of the currents drawn by PLL_1V2 and DVDD.

The plots of the normalized currents for the high-power supplies as a function of the accumulated dose are shown in Figure 7. The measured currents remain essentially constant throughout the irradiation campaign. The only notable change occurs on the 1V8 rail upon switching from the SEU to the TID irradiation runs, where the proton flux is increased (Tables 9 and 10). The current increases by approximately 3%. Since the irradiation profile for Sensor 1 involved switching back to the SEU conditions after the TID dose accumulation, the 1V8 current can be seen to decrease when the proton flux is reduced. However, the current does not return to its pre-TID level, instead stabilizing approximately halfway between the two plateaus. The origin of this behaviour is unclear, as no evidence of a long-term increase in current with accumulated dose is observed.

5.4 Dark current and hot pixels

The increase in pixel dark current with accumulated TID is primarily attributed to the creation of radiation-induced defects in the oxide layers and at the Si–SiO_2 interfaces of the pixel photodiodes and readout circuitry. As ionizing dose accumulates, trapped positive charge and interface states are generated, increasing the surface generation rate of electron–hole pairs. These thermally generated carriers contribute to the dark current, resulting in a gradual increase in the average dark current and in the number of hot pixels. Since the buildup of oxide-trapped charge and interface states is cumulative, the dark current generally increases with the absorbed ionizing dose.

The mean signal level measured by the sensor was monitored between every step of the radiation campaign, by taking $\sim$250 frames with an integrating time of 1 s, with the sensor roughly at 35°C. Unfortunately, complete darkness was not accomplished in the irradiation room and some level of light prevented precise measurement of the dark current. However, it is possible to track the increase of the signal measured by the sensor as a function of the dose, which is presented in Figure 8. The figure shows that a greater proportion of pixels exhibit a higher signal level as the dose is accumulated, which is expected.

The dark current was measured during the pre- and post-radiation characterization campaigns at Nüvü. The post-radiation characterization was performed approximately one month after the completion of the radiation campaign, during which time the devices were stored at room temperature (Figure 9). Consequently, an unknown degree of room-temperature annealing may have occurred, and its contribution to the measured dark current cannot be quantified.

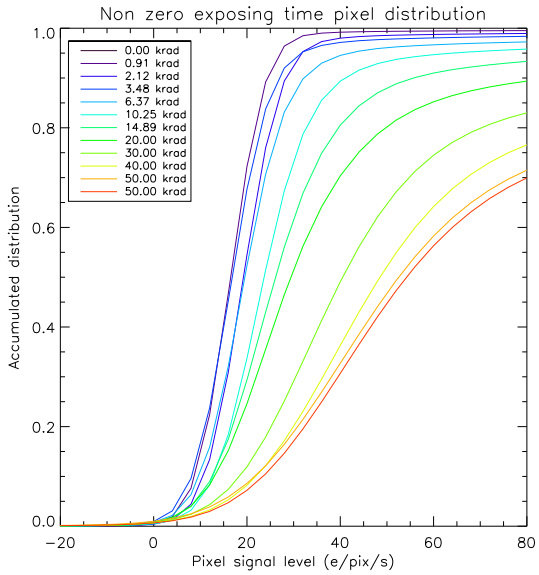

Figure 8: Distribution of the pixel signal for 1,s exposures as a function of the accumulated dose during the irradiation campaign. Since the sensor was not operated in complete darkness, the baseline signal includes both dark current and a contribution from the residual illumination. Consequently, only the increase in the signal with accumulated dose can be attributed to radiation-induced damage to the pixels.

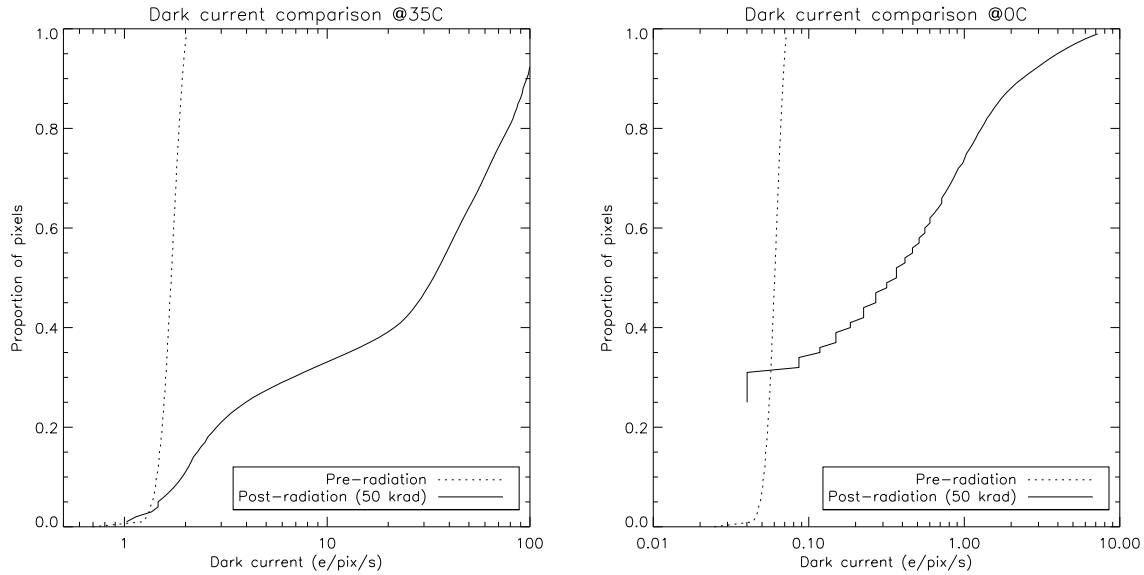

Figure 9: Dark current distribution pre- and post-radiation. **Left**: HWK4123 at 35°C. **Right**: HWK4123 at 0°C.

Nevertheless, since the level of annealing is not known, the results of the characterization post-radiation can be considered as a lower limit of the dark current. In TVAC, the median dark current measured on the irradiated sensor is as shown in Table 14.

The results show that the post-radiation dark current deviates from the expected doubling for every 7°C increase in temperature, particularly at higher operating temperatures. Consequently, the relative increase in dark current due to irradiation decreases as the operating temperature is reduced, with the post- to pre-radiation ratio falling from approximately 20 at 35°C to about 7 at 0°C and -10°C. At 35°C, only 38% of the pixels exhibit a dark current that is less than 10× the

pre-radiation level. At 0°C, that number increases to 63%.

Table 14: Median dark current as a function of the temperature, pre- and post-radiation, for images with 1 s of integration time.

Temperature (°C)	Pre-radiation (ē/pix/s)	Post-radiation (50 krad) (ē/pix/s)
-10	0.02	0.15
0	0.06	0.37
20	0.38	5.90
35	1.69	33.38

5.5 Read-out noise

As for the TVAC characterization, the read-out noise, linearity, and k-gain were measured using the PTC method. A stabilized light source was used to uniformly illuminate the sensor while images were acquired over a range of increasing exposure times, thereby varying the accumulated signal. The illumination level was adjusted such that pixel saturation was reached after approximately 1 s of integration time, while images were acquired up to 2 s. For each integration time, 1000 frames were recorded, providing sufficient statistics to determine the k-gain (ē/ADU), read-out noise, and linearity on a per-pixel basis. Based on repeated PTC acquisitions, this number of frames enables the k-gain to be estimated with a precision better than $\pm$10% for 99.997% of the pixels and better than $\pm$1% for 37.304% of the pixels.

At unity gain, the read-out noise remained unchanged following an accumulated dose of 50 krad (Figure 10, left panel). At a gain of 32, however, the measured temporal noise increases markedly with accumulated dose, with nearly all pixels exhibiting higher post-radiation values. A purely deterministic increase in the dark signal would not explain this behaviour. Instead, the observed increase in temporal variance suggests that radiation-induced defects contribute additional stochastic noise. Proton-induced displacement damage is known to introduce generation-recombination centres within the silicon that increase the mean dark current and may also give rise to Random Telegraph Signal (RTS) noise.[8] Consequently, irradiated pixels can exhibit increased temporal fluctuations in addition to an elevated dark signal. During photon transfer curve measurements, this excess variance contributes to the measured temporal noise floor and, unless the dark-current contribution is independently quantified, may be interpreted as an increase in the apparent read-out noise rather than a degradation of the read-out electronics themselves. Although this interpretation is consistent with the observed behaviour, confirmation would require a dedicated analysis of multi-level RTS noise,[9] which was beyond the scope of the present study.

5.6 Linearity

At unity gain, the linearity of the pixels and of the whole acquisition chain seems to be almost unchanged by the radiations (Figure 11), except close to the saturation of the pixels at their respective gain levels. At gain of 32, the change is more pronounced with the unexpectedly better post-radiation linearity over the 0–200 ē regime.

5.7 k-gain

A ratio of the pre- and post-radiation k-gain distributions is presented in Figure 12. At unity gain, the k-gain shows little sensitivity to radiation, with the 10–90% interval of the distribution remaining within a ratio range of 0.98 to 1.08. At a gain setting of 32, however, the distribution broadens primarily toward higher k-gain values, with 90% of the pixels exhibiting a ratio below 1.22, and still 90% of them showing a ratio greater than 1. This indicates a slight increase in the effective per-pixel k-gain with accumulated dose.

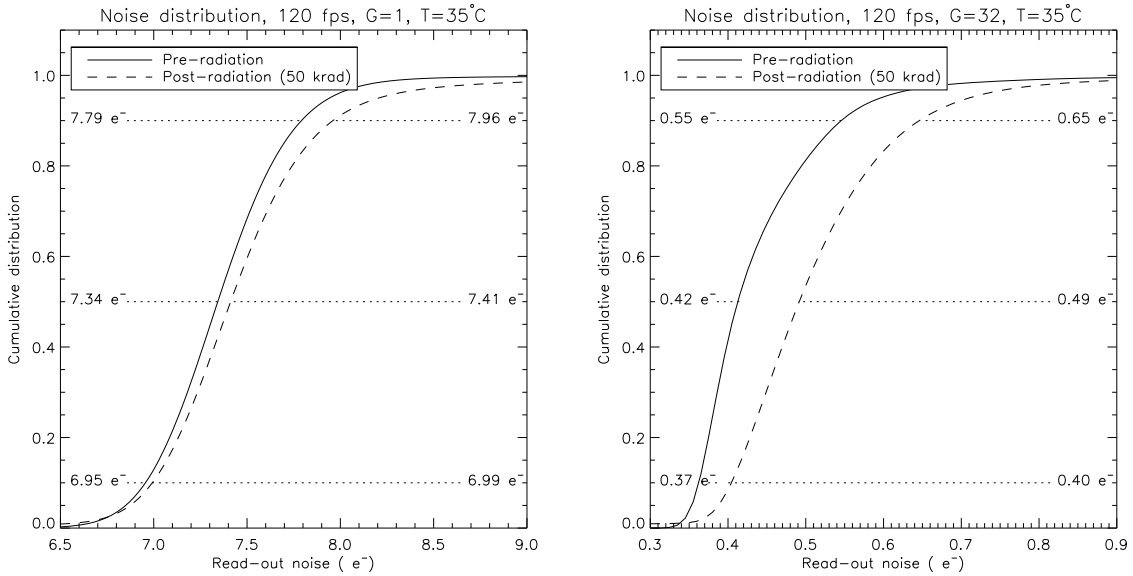

Figure 10: Pre- and post-radiation read-out noise, at a sensor temperature of 35°C. **Left**: Unity gain. **Right**: Gain of 32.

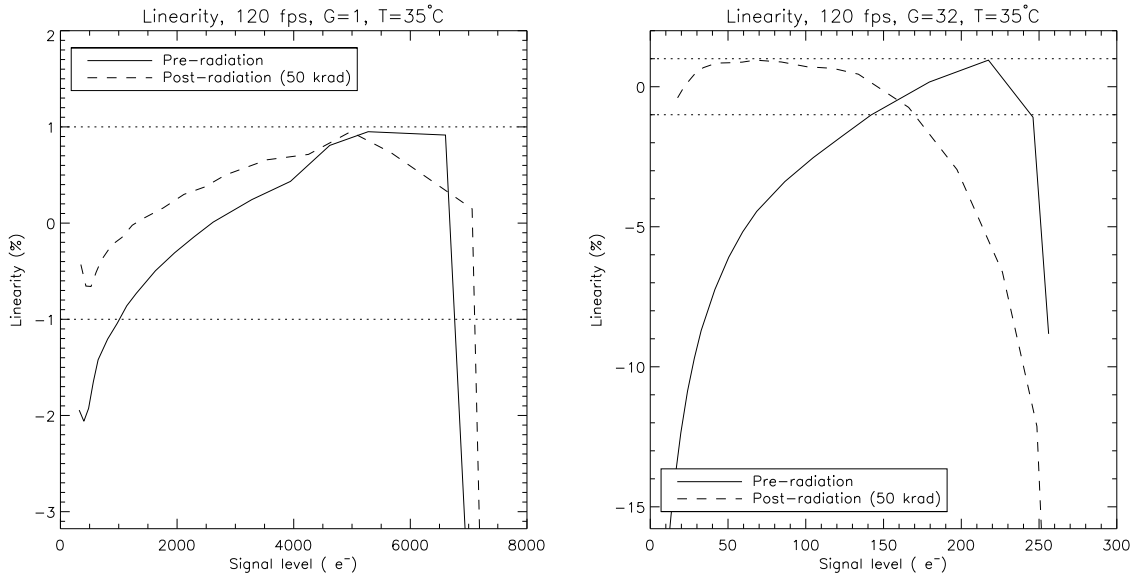

Figure 11: Pre- and post-radiation linearity, at a sensor temperature of 35°C. **Left**: Unity gain. **Right**: Gain of 32.

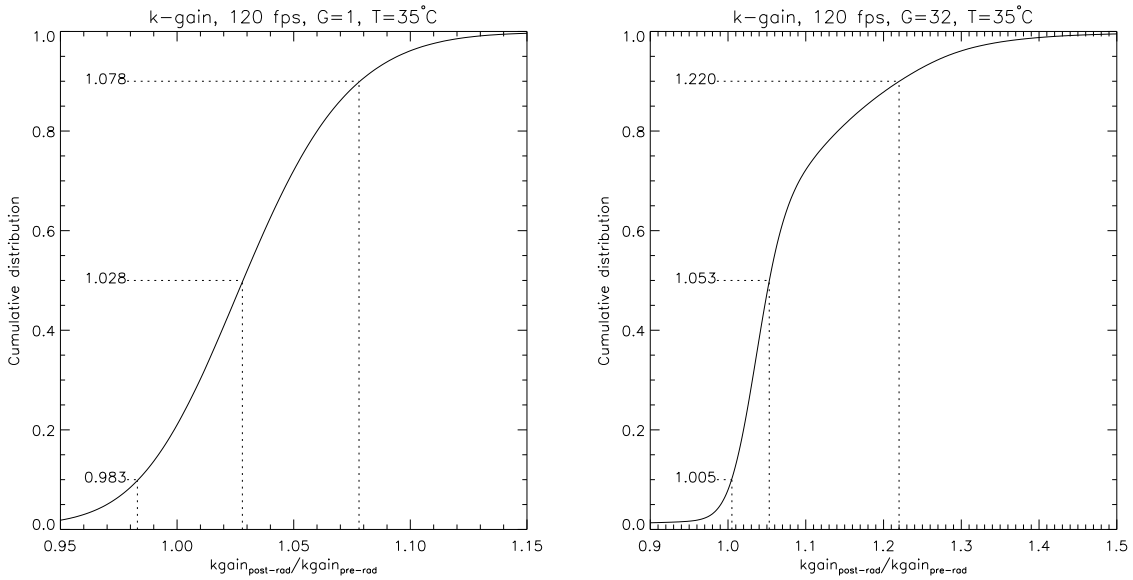

Figure 12: Distribution of the ratios of pre- and post-radiation kgain, at a sensor temperature of 35°C. The figures show the values for 10%, 50% and 90% distributions. **Left**: Unity gain. **Right**: Gain of 32.

6. CONCLUSIONS

Nüvü Camēras' space-qualified digital imaging platform was presented. With its 60 LVDS lines, 34 single-ended I/Os, and 16 high-speed serial receivers dedicated to the imager, together with 12 adjustable low-power DC supplies and 4 high-power (1 A) supplies, it provides a solution with ample resources for driving several types of CMOS and sCMOS image sensors. The first image sensor for which support was developed is the Fairchild's HWK4123.

The HWK4123 is an ultra-low-noise Backside Illuminated (BSI) Scientific CMOS (sCMOS) image sensor featuring a dual-gain 5T pixel architecture, sub-electron read-out noise, low dark current, high dynamic range, and full-frame operation at up to 120 fps. Its unique combination of photon-resolving capability, high full-well capacity, and high frame rate motivated Nüvü Camēras to support the HWK4123 as the first device. The imaging performance achieved with the system is matched to Fairchild's specifications. In Thermal Vacuum Chamber (TVAC), the system was demonstrated to have a stable response across the tested temperature range.

The HWK4123 was tested under proton radiation ranging from 20 to 105 MeV, with an accumulated dose of 50 krad. The sensor remained functional. Although the accumulation of Total Ionizing Dose (TID) increased the dark current of all of the pixels, after 50 krad and at 35°C, 38% of the pixels exhibit a dark current that is less than 10× the pre-irradiation level. At 0°C, that number increases to 63%. The k-gain of the pixels did drift after 50 krad, showing the sensor would require periodic recalibrations as the dose is accumulated to keep an optimal photometric accuracy.

The results of this study demonstrate that Nüvü Camēras' imaging system comprising the space-qualified digital platform and the HWK4123 is well suited for demanding space imaging applications. The results of the irradiation of the sensor showed that it can tolerate the radiation conditions of a LEO environment for several years. Moreover, the platform establishes a versatile foundation for the support of future generations of CMOS and sCMOS image sensors in space.

ACKNOWLEDGMENTS

The research and development was carried out by Nüvü Camēras thanks to the Canadian Space Agency and Innovation, Science and Economic Development Canada programs. Nüvü Camēras made use of the TRIUMF facility to conduct this study.

REFERENCES

[1] Noble, P., "Self-scanned silicon image detector arrays," *Electron Devices, IEEE Transactions on* **15**, 202 – 209 (05 1968).

[2] Fossum, E. R., "Active pixel sensors: are CCDs dinosaurs?," in [*Charge-Coupled Devices and Solid State Optical Sensors III*], Blouke, M. M., ed., **1900**, 2 – 14, International Society for Optics and Photonics, SPIE (1993).

[3] Daigle, O., Djazovski, O., Dupuis, J., Doyon, R., Jahandar, F., Bouguéroua, S., Ducharme, M.-E., Gilbert, A., and Turcotte, J., "Development of a 1U new space camera for EMCCD and CCD sensors with enhanced low-light sensitivity," in [*Sensors, Systems, and Next-Generation Satellites XXVII*], Babu, S. R., Hélière, A., and Kimura, T., eds., **12729**, 127291C, International Society for Optics and Photonics, SPIE (2023).

[4] Bush, N. L., Morrissey, P., Hoenk, M., Kyne, G., Basset, C., Lamborn, A. U., Letona, J. S., Chen, W., Aldrich, D. V., Nemati, B., Gonzalez, G., Williams, P., Daigle, O., Veilleux, J. J., Doyon, F., Shortt, B., and Mackie, R., "Assembly, Optimization and Calibration of the Roman Coronagraph Camera Systems: The Exoplanetary Systems Camera (EXCAM) and the Low Order Wavefront Sensing Camera (LOCAM)," *Journal of Astronomical Telescopes, Instruments, and Systems* **11**(3), 031503 (2025).

[5] Daigle, O., Turcotte, J., Djazovski, O., Gloutnay, É., Grandmont, F., Veilleux, J., Patel, D., and Thibault, S., "TRL-5 EMCCD controller for space applications," in [*Space Telescopes and Instrumentation 2018: Optical, Infrared, and Millimeter Wave*], Lystrup, M., MacEwen, H. A., Fazio, G. G., Batalha, N., Siegler, N., and Tong, E. C., eds., **10698**, 1813 – 1833, International Society for Optics and Photonics, SPIE (2018).

[6] Janesick, J. R., [*Scientific charge-coupled devices*], Scientific charge-coupled devices, Bellingham, WA: SPIE Optical Engineering Press, 2001, xvi, 906 p. SPIE Press monograph, PM 83. ISBN 0819436984 (2001).

[7] Hu, H., "Radiation tolerance of hwk4123 for space applications," tech. rep., Fairchild Imaging, Inc. (Mar. 2026). White paper; Accessed: 2026-05-26.

[8] Antonsanti, A., Virmontois, C., Lauenstein, J.-M., Le Roch, A., Dewitte, H., and Goiffon, V., "Probing dark current random telegraph signal in a small pitch vertically pinned photodiode cmos image sensor after proton irradiation," *IEEE Transactions on Nuclear Science* **69**, 1506–1514 (July 2022).

[9] Goiffon, V., Hopkinson, G. R., Magnan, P., Bernard, F., Rolland, G., and Saint-Pe, O., "Multilevel rts in proton irradiated cmos image sensors manufactured in a deep submicron technology," *IEEE Transactions on Nuclear Science* **56**, 2132–2141 (Aug 2009).